Nanoscale

COMMUNICATION

View Article Online
View Journal | View Issue

Orientation-tuning in self-assembled heterostructures induced by a buffer layer†

Cite this: *Nanoscale*, 2014, **6**, 5126

Received 16th December 2013
Accepted 19th February 2014

DOI: 10.1039/c3nr06664a

www.rsc.org/nanoscale

Yuanmin Zhu,[a] Pingping Liu,[a] Rong Yu,[b] Ying-Hui Hsieh,[c] Dan Ke,[a] Ying-Hao Chu[cd] and Qian Zhan*[a]

Anisotropic nano-plate structures in self-assembled perovskite–spinel thin films, $BiFeO_3$–$NiFe_2O_4$ and $BiFeO_3$–$CoFe_2O_4$, which were deposited on $(001)_c$ $SrRuO_3/SrTiO_3$ and $DyScO_3$ substrates, respectively, have been demonstrated using transmission electron microscopy combined with strain analysis. Unlike the unitary cube-on-cube orientation relationship reported widely, the growth direction of the $CoFe_2O_4$ and $NiFe_2O_4$ plates was tuned to $[011]_c$ while the $BiFeO_3$ matrix kept $[001]_c$ in both systems. In particular, a thin stress-sensitive $BiFeO_3$ buffer layer between the spinel nanostructure and the substrate was introduced for providing a complex strain state in both film systems. The novel orientation tuning and the pattern configuration of the heterostructures are mainly attributed to the strain imposed on the films and the anisotropic ledge growth mechanism of spinels.

1. Introduction

Complex oxides cover a wide range of intriguing functionalities induced by interplay among the lattice, charge, orbitals and spin degrees of freedom and offer tremendous opportunities to develop next generation electronic devices.[1–3] Among complex oxide heterostructures, the vertical nanocomposite architecture has drawn considerable attention and has been used to tune functionalities benefitting from their plentiful hetero-interfaces, *e.g.* $BiTiO_3$–$CoFe_2O_4$, $BiFeO_3$–$CoFe_2O_4$,[4,5] $PbTiO_3$–$CoFe_2O_4$,[6] $BiTiO_3$–Sm_2O_3,[7] $La_{0.7}Sr_{0.3}MnO_3$–CeO_2 (ref. 8) *etc.* The unique physical properties of materials can be tuned through structure modification which is a fundamental topic often addressed.

The thermodynamics and kinetics affecting the evolution of these nanostructures are various and complicated, such as elastic energy, crystal structure, interface energy, growth parameters and heat treatment.[9–13] For epitaxial thin films, elastic strain energy, commonly induced by the epitaxial constraints along the heterointerfaces due to lattice mismatch, is demonstrated to be a vital factor controlling the growth of heterostructures.[14,15] The strain affects the chemical bond length and angles, defect types and densities such as dislocation and oxygen vacancies, thus manipulating the corresponding physics of the nanostructures.[16] Through theoretical and experimental investigations of the classic vertical nanostructures, Roytburd *et al.* suggested a general way of controlling the phase architectures by elastic interactions between substrates and films.[17,18] Previous studies mainly focused on the vertical heterostructures with a simple cube-on-cube orientation relationship between the constituent phases and the substrate, that is [001]//[001] and (100)//(100).[19–25] Recently, a significant attempt was made to control the relative orientations in the two-phase heterostructures by strain engineering using substrates with different crystal structures and lattice parameters.[26] Exploring wider manipulations for crystallographic orientations and hetero-interfaces in complex oxide vertical nanostructures has become extremely important.

In the present paper, rather than the unitary cube-on-cube crystallographic orientations, periodic plate-configurations of two-phase nanostructures induced by a buffer layer were observed by transmission electron microscopy (TEM). Perovskite $BiFeO_3$ (BFO) and spinel $NiFe_2O_4$ or $CoFe_2O_4$ (NFO, CFO) self-assembled heteroepitaxial nanostructures were chosen as the model systems. The interfacial structures at an atomic scale and the underlying growth mechanisms were discussed in detail. Two key points have to be emphasized to realize the controllable orientation tuning by strain engineering in vertical heterostructure thin films. First of all, a buffer layer of BFO, which has been demonstrated to have high stress sensitivity in

[a]*School of Materials Science and Engineering, University of Science and Technology Beijing, Beijing 100083, China. E-mail: qzhan@mater.ustb.edu.cn*

[b]*Beijing National Center for Electron Microscopy, Department of Materials Science and Engineering, Tsinghua University, Beijing 100084, China. E-mail: Ryu@tsinghua.edu.cn*

[c]*Department of Materials Science and Engineering, National Chiao Tung University, Hsinchu 30010, Taiwan. E-mail: yhc@nctu.edu.tw*

[d]*Institute of Physics, Academia Sinica, Taipei 105, Taiwan*

† Electronic supplementary information (ESI) available: A schematic of the 3-D relationships in the perovskite–spinel systems and the related HRTEM images are available. See DOI: 10.1039/c3nr06664a

many pioneering works,[27–29] was introduced to tune the orientation of the nanostructures. Secondly, perovskite substrates with lattice parameters close to BFO were selected in order to facilitate highly coherent heteroepitaxial strain in BFO.

2. Experimental

Perovskite–spinel $BiFeO_3$–$NiFe_2O_4$ and $BiFeO_3$–$CoFe_2O_4$ heteroepitaxial nanostructures were grown on single crystal $(001)_c$ $SrTiO_3$ and $(001)_c$ $DyScO_3$ substrates, respectively, by pulsed laser deposition at 700 °C under an oxygen pressure of 200 mTorr (subscript c represents a cubic/pseudocubic structure). Both composite targets were produced with a molar ratio of 0.65BFO : 0.35NFO/CFO. BFO has a rhombohedrally distorted perovskite structure with a *R3c* space group that can be described as a pseudocubic cell, $a_c = 3.962$ Å.[30] NFO and CFO are magnetic spinels with cubic *Fd3m* structures ($a_{NFO} = 8.34$ Å, $a_{CFO} = 8.38$ Å).[31,32] BFO–CFO and BFO–NFO systems show similar structural characteristics,[21] thus the results are discussed together in the present study. The $SrTiO_3$ (STO) substrate for the growth of the BFO–NFO film has a cubic perovskite structure, on which a 30 nm thick $SrRuO_3$ (SRO) epilayer was grown for decreasing the lattice mismatch with BFO. The strain in the 30 nm thick SRO layer was relaxed to a large extent which was estimated from the critical thickness. SRO has lattice parameters of $a_o = 5.5943$ Å, $b_o = 5.5708$ Å and $c_o = 7.8810$ Å (pseudocubic lattice $a_c = 3.9405$ Å (ref. 33)) (subscript o represents an orthorhombic structure). $DyScO_3$ (DSO) with lattice parameters of $a_o = 5.4494$ Å, $b_o = 5.7263$ Å and $c_o = 7.9132$ Å ($a_c = 3.940$ Å (ref. 34)) was chosen to be the substrate for another similar system of a BFO–CFO nanocomposite film. DSO and SRO as the direct contact surfaces for the growth of the films have orthorhombic (*Pbnm* 62) distorted perovskite structures, having a nominal misfit of ~0.55% with the BFO matrix. The following indexing and discussion on the perovskite structures refer to the pseudo-cubic unit cell for simplicity.

Cross-section as well as plan-view samples for TEM were prepared by a standard procedure of TEM sample preparation. Macro- and microstructures of the films were investigated using an FEI TECNAI F20 microscope with an information limit of 1.4 Å, a Philips CM300 microscope with a point resolution of 1.7 Å and information resolution of 0.8 Å and a JEOL-2010 microscope operating at 200 kV. Chemical analysis was also carried out using the F20 microscope equipped with an Energy Dispersive X-Ray Detector (EDX).

3. Results and discussion

The low magnification morphologies and corresponding electron diffraction patterns (EDPs) of the self-assembled BFO–NFO nanostructures grown on (001)-oriented SRO/STO substrates are given in Fig. 1. Two dimensional (2-D) maze-like NFO nanostructures were embedded homogeneously in the BFO matrix, as shown in Fig. 1a and c. Plate-shaped NFO elongated along the $\langle 011\rangle_{NFO}$ direction with an average length (L) of ~450 nm and width (W) about 35 nm, making the aspect ratio of L/W around 13. These nanostructures grew perpendicularly to the substrate

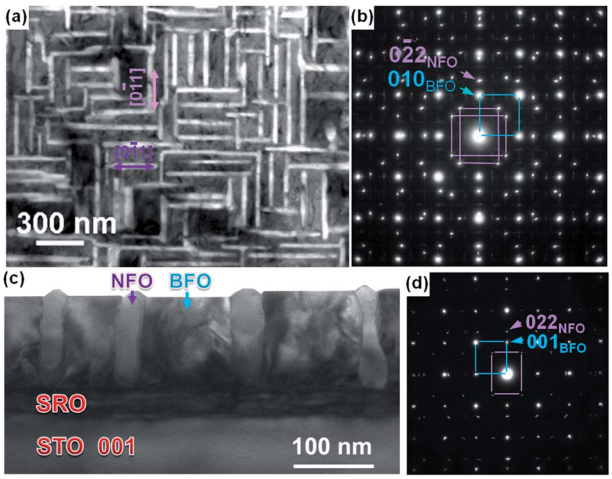

Fig. 1 (a) Plan-view TEM image of the BFO–NFO nanostructure and (b) the corresponding diffraction pattern. (c) Cross-sectional TEM image showing NFO inclusions embedded in the BFO matrix of films grown on a (001) STO substrate with a ~30 nm thick SRO transition layer. (d) Selected area diffraction pattern from (c) with a [010] BFO direction.

and exhibited a vertical interface with the BFO matrix. $\{111\}_{NFO}$ facets formed out of the film surface for nanostructured NFO, which is confirmed by the following high resolution transmission electron microscopy (HRTEM) image. As seen from the plan-view EDP (Fig. 1b), the two sets of mutually perpendicular [011]-oriented patterns of the NFO phase were determined to be [011](0−22)NFO//[001](010)BFO//[001](010)STO and [011](0−22)NFO//[001](100)BFO//[001](100)STO, in accordance to the 2-D morphology revealed in Fig. 1a. The cross-sectional EDP in Fig. 1d demonstrates that the BFO matrix kept the $[001]_c$ growth direction matching the $[001]_c$ orientated perovskite substrate, while the NFO plate was tuned to $[011]_{NFO}$, obtaining the out-of plane orientation relationship of [0−11](022)NFO//[010](001)BFO//[010](001)STO. The vertical interface between the BFO and NFO phases lies on the {100} NFO/{100} BFO planes. It's clear that the pattern configuration and the crystallographic orientation of the NFO nanostructures in this typical perovskite–spinel system are different from previous studies.

Fig. 2a and c show the configuration of the $BiFeO_3$–$CoFe_2O_4$ nanocomposite thin films from both plan-view and cross-section orientations. They were grown on $(001)_c$ single crystal DSO substrates that have an orthorhombic distorted perovskite structure. $CoFe_2O_4$, having the same spinel structure as NFO, was found to be included in the $BiFeO_3$ matrix. Unlike the above 2-D BFO–NFO system, however, the CFO nanostructures elongated only along one direction of $[0-11]_{CFO}/[010]_{BFO}$ and exhibited short and thick rectangular shapes with an aspect ratio (L/W) of 2.83. The growth direction of CFO was along $[011]_{CFO}$ while the BFO matrix remained along the $[001]_c$ orientation, the same as the above BFO–NFO/SRO/STO system. $\{111\}_{CFO}$ facets and {100} vertical interfaces were also observed in the BFO–CFO/DSO thin films. The orientation relationships between BFO and CFO as well as the DSO substrate can

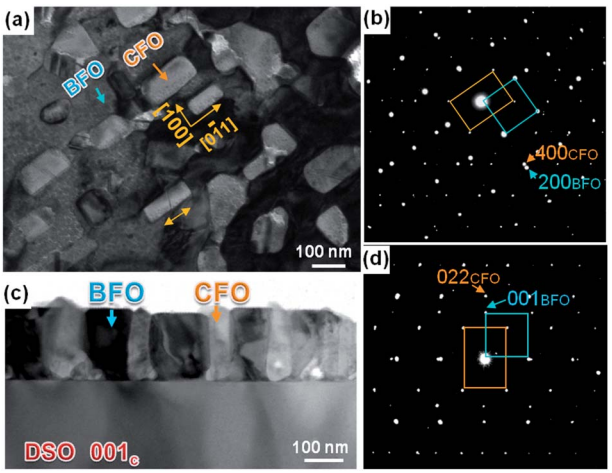

Fig. 2 Typical TEM morphologies of the $BiFeO_3$–$CoFe_2O_4$ thin film grown on a $DyScO_3$ substrate, (a) plan-view from the [001]BFO/[011] CFO direction and (c) cross-section of the CFO [0−11] direction. (b) and (d) show the corresponding electron diffraction patterns of the plan-view (a) and cross-section (c), respectively.

be determined to be [011](0−22)CFO//[001](010)BFO//[001](010)$_c$DSO for the in plane [Fig. 2b] and [0−11](022)CFO//[010](001)BFO//[010](001)$_c$DSO for the out of plane direction (Fig. 2d).

On the (001)$_c$ SRO/STO and DSO perovskite surfaces, the [011]$_{CFO/NFO}$-orientated CFO/NFO nanostructures can be observed in both systems with the BFO matrix keeping the [001]$_c$ growth direction, demonstrating novel nanostructure configurations and crystal growth model. Note that the NFO and CFO nanostructures preferred to elongate along the ⟨110⟩ direction. Such growth behavior for the spinel structure can be ascribed to ledge preferential growth induced by the anisotropic arrangement of cations along the ⟨110⟩ direction in the spinel structure.[35] Meanwhile, a distinct difference was observed in the two similar systems: one dimensional and 2-D plate distributions of the nanostructures with different aspect ratios developed in the BFO–CFO/DSO and BFO–NFO/SRO/STO systems, respectively. Intrinsic microstructural features should be investigated further to reveal such an unusual phenomenon.

To shed light on the intriguing growth of the nanostructures, HRTEM was carried out to show the interface structure at an atomic scale. The interface structure between the NFO/CFO plates and BFO matrix as well as with the substrates is shown in Fig. 3. The incident beam was along the [0−11]$_{NFO/CFO}$/[010]$_{BFO}$ direction. Well-defined vertical interfaces between the two constituent phases lay on the {100} planes in both systems (Fig. 3a and b). Both spinel NFO and CFO plates formed {111} facets at the film surface whereas the perovskite BFO matrix exhibits a (001) flat surface since the lowest surface energy differs with different crystal structures.[36,37] Moreover, the lattice mismatch between the BFO matrix and vertical CFO/NFO nanostructures was almost relaxed at their interfaces in the present study (see Fig. S3†), which is consistent with our previous studies.[12,21]

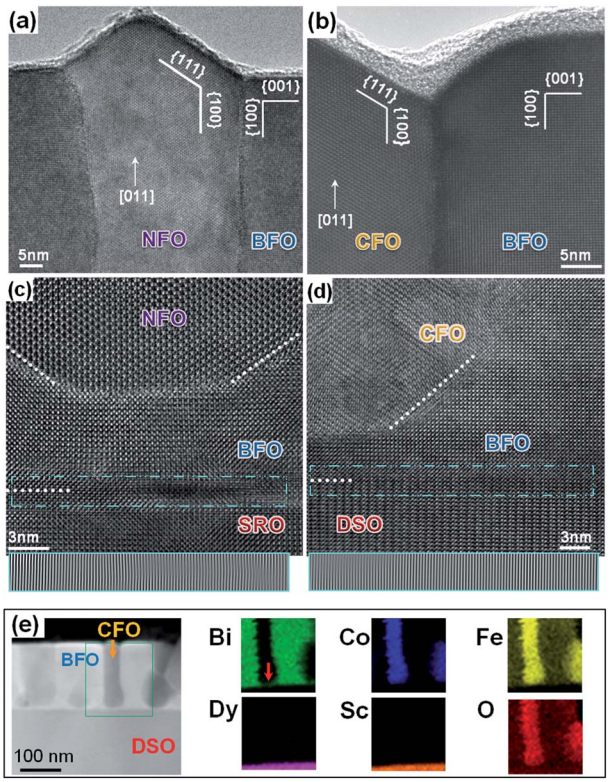

Fig. 3 High resolution cross-sectional images of the BFO–CFO/NFO films on different substrates. (a) and (b) BFO–NFO interface at the film surface and BFO–CFO interface at the film surface, respectively. (c) NFO–BFO–SRO interfaces close to the substrate showing a 7 nm thick-BFO layer coherent with the SRO surface but semi-coherent with the NFO phase. (d) CFO–BFO–DSO interface, showing a thin BFO layer of 4 nm. The bottom insets in (c) and (d) are one-dimensional FFT filtered images of the dashed boxes. (e) EDS data of the BFO–CFO films grown on a DSO substrate showing the cross-sectional HAADF image and the corresponding elemental maps of Bi, Co, Fe, Dy, Sc and O obtained from the area marked by a green square.

In particular, a thin BFO buffer layer between the composite thin film and the substrate was revealed in both cases. The thicknesses of the BFO thin layers were about 7 nm on SRO/STO and 4 nm on DSO, as shown in Fig. 3c and d. The results of energy-dispersive X-ray spectroscopy (EDS) agreed well with the HRTEM observations. Taking BFO–CFO on the DSO substrate as an example, the composition distribution mapping is given in Fig. 3e. An underlying thin layer containing Bi, Fe and O between the CFO and DSO substrates was clearly observed. Thus, the spinel phases of CFO/NFO did not grow on the substrate surface directly but were embedded in the BFO matrix wholly as included plates. The interfaces between the clamped BFO thin layers and substrates marked by blue boxes in the figures were Fourier-filtered along the [100] direction, as shown at the bottom of Fig. 3c and d, respectively. The hetero-interfaces were almost coherent, revealing a high strain state present in the BFO buffer layer.

Quantitative analysis on the local strain state in the vicinity of the BFO–substrate heterointerfaces is shown in Fig. 4 and the standard deviations are also given. Although experimental errors existed, the relative variations of the lattices reveal the

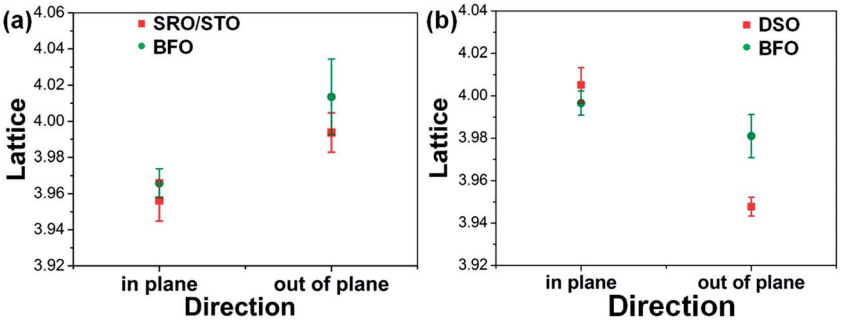

Fig. 4 Lattice parameters measured at the bottom interfaces of (a) BFO–SRO/STO and (b) BFO–DSO in both systems from the cross-sectional HRTEM images.

complex strain state in the film systems. There are few differences in the in-plane lattice parameters between the strained-BFO layer and the SRO/STO (Fig. 4a) and DSO substrates (Fig. 4b). The thin buffer layer of BFO was subjected to in-plane compressive stress when grown on the SRO/STO substrate and tensile stress on the DSO substrate. The relative misfit can be measured to be −0.24% and 0.22% respectively, where the negative sign (−) represents compressive stress. On the other hand, the out-of plane lattice parameters of BFO in the vicinity of the interfaces increased when it was grown on the SRO/STO substrate and decreased when deposited on the DSO substrate, consistent with the analysis of the in-plane strain state expected from the lattice mismatch. Such a complex strain state owing to the highly clamped underlying BFO thin layers could be responsible for the unusual arrangement of the CFO/NFO nanostructures. One important fact that should be emphasized is that the clamped layer was rarely reported in the typical perovskite–spinel nanocomposite films epitaxially grown on (001) STO substrates in previous studies, such as BFO–CFO, BTO–CFO, BFO–NFO and PTO–CFO with cube-on-cube relationships.[19–23,36] Therefore, we focused on the strained BFO buffer layer in the subsequent discussion, which is a significant aspect that shouldn't be neglected when considering the orientation control in the spinel nanostructures.

In vertical nanostructure systems, many factors may affect the pattern configurations during heteroepitaxial growth, such as thermodynamic and kinetic ones (*e.g.* elastic energy, the anisotropy of chemical bonds in the crystal structures, interface energy, surface energy and growth parameters, *etc.*), among which the epitaxial strain originating from the mismatch between films and substrates and the crystal structure of substrates play a key role in determining the growth behavior of the nanostructures. We know that rhombohedral distorted perovskite BFO is extremely sensitive to stress, which can reveal its ability to undergo a morphotropic phase transition due to epitaxial strain.[27–29] The combination of strain-sensitive BFO and substrates with different anisotropies associated with crystal structure would impose a complex strain state on the included nanostructures which may affect their nucleation and dynamic growth behavior. A possible growth mechanism is proposed based on the experimental observations and the strain state analysis for the present study. Fig. 5 schematically shows the formation of [011] orientated nanostructures in the two film systems by three stages of growth.

With the fluctuation in deposition conditions of the films at the initial growth stage (Fig. 5a), for example a small increase in deposition rate or temperature, it's reasonable to presume that crystalline BFO prefers to wet the surface of the substrate and spread quickly since it has the same perovskite structure and a lower nucleation barrier on the perovskite substrate. Meanwhile, the spinel phase won't start to nucleate immediately for two main reasons. One is the large structural difference between the cubic spinel and the orthorhombically distorted perovskite substrate. Another point lies in that the polyhedral spinel crystal with low surface reconstruction energy needs some time to collect a certain amount of spinel species.[38] Therefore, thin BFO buffered layers formed coherently on the surface of the substrates at the early stage of deposition (Fig. 5b), which can be observed in Fig. 3c and d. A key question regarding strain thus arises: can the misfit strain in the BFO buffered layer be released by the formation of dislocations or not? For heteroepitaxial thin films, the calculated critical thickness for forming misfit dislocations can be described by the following formula based on Matthews' and Blakeslee's theory:[39,40]

$$h_c = \frac{b}{8\pi(1+\nu)f}\left[\ln\left(\frac{h_c}{b}\right)+1\right] \quad (1)$$

where ν is Poisson's ratio, f is the relative misfit, and b is the Burgers vector of misfit dislocations. Setting $\nu = 0.25$, a typical value for oxides,[39] the Burgers vector b can be considered to be $a_{[010]}$ of the substrate (~0.394 nm) and h_c is estimated to be about 9.4 nm for the ~0.55% nominal mismatch of BFO and DSO or SRO. Thus, the thickness of the BFO buffer layer in the present study, which is less than 7 nm in both systems, did not exceed the critical thickness as in the theoretical prediction. Therefore, the BFO thin layer is clamped by the substrate almost coherently, suggesting that it is under a state of biaxial tensile/compressive constraint imposed by the heteroepitaxy. Therefore, octahedral tilting and rotation in the orthorhombic distorted perovskite substrates can easily impact on the BFO thin layer.

As the deposition process continues at a high temperature of 700 °C, the spinel nucleus of NFO/CFO might aggregate and start to grow on the surface of the highly strained BFO buffer

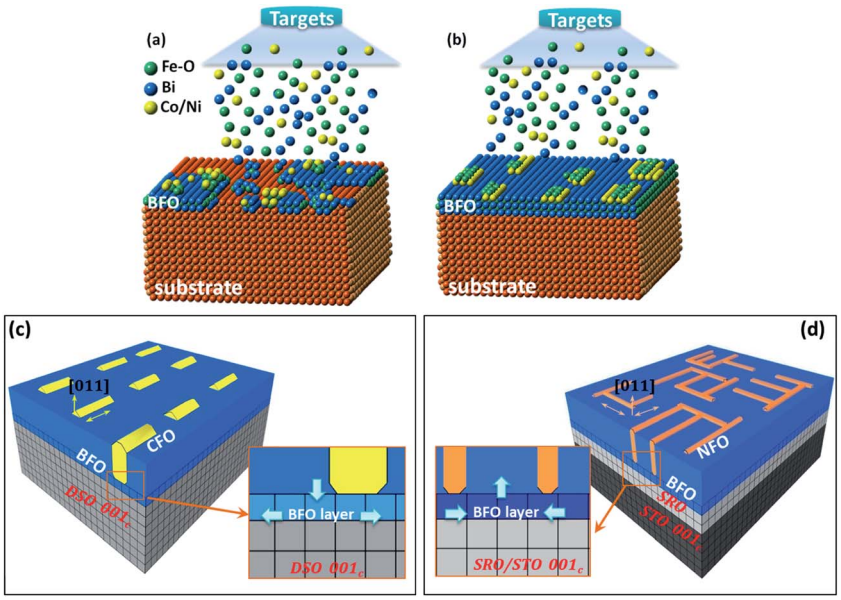

Fig. 5 Schematic model of the growth procedure with three deposition stages. (a) Thin BFO phase wetting the substrates. (b) Spinel phase nucleation on the BFO buffer layers. (c) CFO nano-plate islands form in the BFO matrix. (d) NFO nano-plates form in the BFO matrix. The enlarged insets of (c) and (d) show the coherent BFO buffer layer and the corresponding strain state analysis from Fig. 4.

layer, as shown in Fig. 5b. The crystals of NFO/CFO elongated along the ⟨0−11⟩ in-plane directions due to the preferential motion of the spinel ledges with lower activation energy, which is called the ledge growth mechanism.[35] On the other hand, the orthorhombically distorted DSO substrate provides an anisotropic characteristic and octahedron distortion. It can apply a similar anisotropic stress on the above BFO thin layer which results in the in-plane unequivalent stress in BFO even if it is equivalent in the bulk structure. Correspondingly, the above CFO elongated along one of its ⟨110⟩ directions and formed an anisotropic nano-plate structure with the [011] orientation, as shown in Fig. 5c. A 2-D nanostructure, however, was observed when similar BFO–NFO composite films grew on the SRO/STO substrate. The in-plane anisotropy of SRO is much smaller than that of DSO by comparison of their lattice parameters. Therefore, the clamped BFO and hence the above NFO nanostructure grew along two ⟨110⟩ directions, creating 2-D structural variants perpendicular to each other (Fig. 5d).

Anisotropic elongation of the vertical nanostructures and regulations on the crystallographic orientation may provide many choices for designing strong correlated complex oxides. The tunable nanostructures may enable the control of material functionalities such as the magnetic anisotropy of CFO with a fixed elongation direction, which would demonstrate a great potential application in next generation electromagnetic devices.

4. Conclusions

In summary, we have demonstrated the nano-plate configurations with defined heterointerface structures and misorientation relationships in the $BiFeO_3$–$CoFe_2O_4$ and $BiFeO_3$–$NiFe_2O_4$ perovskite–spinel model systems when grown on $[001]_c$ oriented SRO/STO and DSO substrates, respectively. The spinel nano-plates, elongated along the $\langle 110\rangle_{NFO/CFO}$ directions with anisotropic distributions, were fully embedded in the BFO matrix and their crystal orientations were tuned to [011] along the growth direction, with BFO keeping the cube-on-cube orientation relationship with the perovskite substrates. A highly strained thin BFO buffer layer was introduced between the spinel plates and the substrates to determine the initial growth of the spinel nano-plates. Manipulation of the vertical nanostructures in both film systems can be attributed to the complicated strain state in the film systems and the preferential motion of the spinel structures along the ⟨110⟩ ledges.

Acknowledgements

This work is supported by the program of National Basic Research Development Plan with Grant no. 2011GB108002, 2011CB606406, and the National Natural Science Foundation of China with Grant no. 51371031, 50971015, 51071092. The work in National Chiao Tung University is supported by the National Science Council, R.O.C. (NSC-101-2119-M-009-003-MY2), Ministry of Education, R.O.C. (MOE-ATU 101W961), and Center for interdisciplinary science of National Chiao Tung University. The authors gratefully acknowledge Professor R. Ramesh and Dr S. P. Crane of the University of California, Berkeley for their provision of a part of the samples and the support from the National Center for Electron Microscopy, Lawrence Berkeley National Laboratory.

Notes and references

1 S. Wu, S. A. Cybart, P. Yu, M. Rossell, J. Zhang, R. Ramesh and R. Dynes, *Nat. Mater.*, 2010, **9**, 756–761.

2 J. L. MacManus-Driscoll, *Adv. Funct. Mater.*, 2010, **20**, 2035–2045.
3 L. W. Martin and R. Ramesh, *Acta Mater.*, 2012, **60**, 2449–2470.
4 H. Zheng, J. Wang, S. E. Lofland, Z. Ma, L. Mohaddes-Ardabili, T. Zhao, L. Salamanca-Riba, S. R. Shinde, S. B. Ogale, F. Bai, D. Viehland, Y. Jia, D. G. Schlom, M. Wuttig, A. Roytburd and R. Ramesh, *Science*, 2004, **303**, 661–663.
5 Y.-J. Chen, Y.-H. Hsieh, S.-C. Liao, Z. Hu, M.-J. Huang, W.-C. Kuo, Y.-Y. Chin, T.-M. Uen, J.-Y. Juang, C.-H. Lai, H.-J. Lin, C.-T. Chen and Y.-H. Chu, *Nanoscale*, 2013, **5**, 4449–4453.
6 J. Li, I. Levin, J. Slutsker, V. Provenzano, P. K. Schenck, R. Ramesh, J. Ouyang and A. L. Roytburd, *Appl. Phys. Lett.*, 2005, **87**, 072909.
7 S. A. Harrington, J. Zhai, S. Denev, V. Gopalan, H. Wang, Z. Bi, S. A. T. Redfern, S. H. Baek, C. W. Bark and C. B. Eom, *Nat. Nanotechnol.*, 2011, **6**, 491–495.
8 A. Chen, Z. Bi, H. Hazariwala, X. Zhang, Q. Su, L. Chen, Q. Jia, J. L. MacManus-Driscoll and H. Wang, *Nanotechnology*, 2011, **22**, 315712.
9 W. Chang, J. S. Horwitz, A. C. Carter, J. M. Pond, S. W. Kirchoefer, C. M. Gilmore and D. B. Chrisey, *Appl. Phys. Lett.*, 1999, **74**, 1033.
10 Z. Bi, E. Weal, H. Luo, A. Chen, J. L. MacManus-Driscoll, Q. Jia and H. Wang, *J. Appl. Phys.*, 2011, **109**, 054302.
11 N. Dix, R. Muralidharan, J. M. Rebled, S. Estradé, F. Peiró, M. Varela, J. Fontcuberta and F. Sánchez, *ACS Nano*, 2010, **4**, 4955.
12 Y. M. Zhu, D. Ke, R. Yu, Y. H. Hsieh, H. J. Liu, P. P. Liu, Y. H. Chu and Q. Zhan, *Appl. Phys. Lett.*, 2013, **102**, 111903.
13 B. Mercey, M. Hervieu, W. Prellier, J. Wolfman, C. Simon and B. Raveau, *Appl. Phys. Lett.*, 2001, **78**, 3857.
14 D. G. Schlom, L.-Q. Chen, C.-B. Eom, K. M. Rabe, S. K. Streiffer and J.-M. Triscone, *Annu. Rev. Mater. Res.*, 2007, **37**, 589–626.
15 A. Mukherjee, W. S. Cole, P. Woodward, M. Randeria and N. Trivedi, *Phys. Rev. Lett.*, 2013, **110**, 157201.
16 J. Gazquez, S. Bose, M. Sharma, M. A. Torija, S. J. Pennycook, C. Leighton and M. Varela, *APL Mater.*, 2013, **1**, 012105.
17 A. Artemev, J. Slutsker and A. L. Roytburd, *Acta Mater.*, 2005, **53**, 3425–3432.
18 J. Slutsker, I. Levin, J. Li, A. Artemev and A. Roytburd, *Phys. Rev. B: Condens. Matter Mater. Phys.*, 2006, **73**, 184127.
19 I. Levin, J. Li, J. Slutsker and A. L. Roytburd, *Adv. Mater.*, 2006, **18**, 2044–2047.
20 Z. Tan, J. Slutsker and A. L. Roytburd, *J. Appl. Phys.*, 2009, **105**, 061615.
21 Q. Zhan, R. Yu, S. P. Crane, H. Zheng, C. Kisielowski and R. Ramesh, *Appl. Phys. Lett.*, 2006, **89**, 172902.
22 I. Fina, N. Dix, L. Fàbrega, F. Sánchez and J. Fontcuberta, *J. Appl. Phys.*, 2010, **108**, 034108.
23 H. Zheng, F. Straub, Q. Zhan, P. L. Yang, W. K. Hsieh, F. Zavaliche, Y. H. Chu, U. Dahmen and R. Ramesh, *Adv. Mater.*, 2006, **18**, 2747–2752.
24 H. Zheng, J. Wang, L. Mohaddes-Ardabili, M. Wuttig, L. Salamanca-Riba, D. G. Schlom and R. Ramesh, *Appl. Phys. Lett.*, 2004, **85**, 2035.
25 N. M. Aimon, D. Hun Kim, H. Kyoon Choi and C. A. Ross, *Appl. Phys. Lett.*, 2012, **100**, 092901.
26 S. C. Liao, P. Y. Tsai, C. W. Liang, H. J. Liu, J. C. Yang, S. J. Lin, C. H. Lai and Y. H. Chu, *ACS Nano*, 2011, **5**, 4118–4122.
27 R. J. Zeches, M. D. Rossell, J. X. Zhang, A. J. Hatt, Q. He, C. H. Yang, A. Kumar, C. H. Wang, A. Melville, C. Adamo, G. Sheng, Y. H. Chu, J. F. Ihlefeld, R. Erni, C. Ederer, V. Gopalan, L. Q. Chen, D. G. Schlom, N. A. Spaldin, L. W. Martin and R. Ramesh, *Science*, 2009, **326**, 977–980.
28 I. C. Infante, S. Lisenkov, B. Dupé, M. Bibes, S. Fusil, E. Jacquet, G. Geneste, S. Petit, A. Courtial, J. Juraszek, L. Bellaiche, A. Barthélémy and B. Dkhil, *Phys. Rev. Lett.*, 2010, **105**, 057601.
29 J. Yang, Q. He, S. Suresha, C. Kuo, C. Peng, R. Haislmaier, M. Motyka, G. Sheng, C. Adamo and H. Lin, *Phys. Rev. Lett.*, 2012, **109**, 247606.
30 J. Moreau, C. Michel, R. Gerson and W. James, *J. Phys. Chem. Solids*, 1971, **32**, 1315–1320.
31 K. Subramanyam, *J. Phys. C: Solid State Phys.*, 1971, **4**, 2266.
32 A. Goldman, *Modern Ferrite Technology*, Springer, 2006, p. 55.
33 B. J. Kennedy and B. A. Hunter, *Phys. Rev. B: Condens. Matter Mater. Phys.*, 1998, **58**, 653–658.
34 ICDD Grand-in-Aid 1974 (X-ray data base file ID: 27-0204), Penn State University, University Park, Pennsylvania.
35 S. V. Yanina and C. Barry Carter, *Surf. Sci.*, 2002, **513**, L402–L412.
36 H. Zheng, Q. Zhan, F. Zavaliche, M. Sherburne, F. Straub, M. P. Cruz, L. Q. Chen, U. Dahmen and R. Ramesh, *Nano Lett.*, 2006, **6**, 1401–1407.
37 G. Wulff, *Z. Kristallogr. Mineral.*, 1901, **34**, 449–530.
38 Y.-H. Hsieh, H.-H. Kuo, S.-C. Liao, H.-J. Liu, Y.-J. Chen, H.-J. Lin, C.-T. Chen, C.-H. Lai, Q. Zhan, Y.-L. Chueh and Y.-H. Chu, *Nanoscale*, 2013, **5**, 6219.
39 X. Qi, M. Wei, Y. Lin, Q. Jia, D. Zhi, J. Dho, M. G. Blamire and J. L. MacManus-Driscoll, *Appl. Phys. Lett.*, 2005, **86**, 071913.
40 J. Matthews and A. Blakeslee, *J. Cryst. Growth*, 1974, **27**, 118–125.